PAPER

CrossMark
←click for updates

Evidence for 5d-σ and 5d-π covalency in lanthanide sesquioxides from oxygen K-edge X-ray absorption spectroscopy†

Alison B. Altman,[a,b] Joseph I. Pacold,[b] Jian Wang,[c] Wayne W. Lukens[b] and Stefan G. Minasian*[b]

The electronic structure in the complete series of stable lanthanide sesquioxides, Ln_2O_3 (Ln = La to Lu, except radioactive Pm), has been evaluated using oxygen K-edge X-ray absorption spectroscopy (XAS) with a scanning transmission X-ray microscope (STXM). The experimental results agree with recent synthetic, spectroscopic and theoretical investigations that provided evidence for 5d orbital involvement in lanthanide bonding, while confirming the traditional viewpoint that there is little Ln 4f and O 2p orbital mixing. However, the results also showed that changes in the energy and occupancy of the 4f orbitals can impact Ln 5d and O 2p mixing, leading to several different bonding modes for seemingly identical Ln_2O_3 structures. On moving from left to right in the periodic table, abrupt changes were observed for the energy and intensity of transitions associated with Ln 5d and O 2p antibonding states. These changes in peak intensity, which were directly related to the amounts of O 2p and Ln 5d mixing, were closely correlated to the well-established trends in the chemical accessibility of the 4f orbitals towards oxidation or reduction. The unique insight provided by the O K-edge XAS is discussed in the context of several recent theoretical and physical studies on trivalent lanthanide compounds.

Introduction

A comprehensive model of 4f and 5d orbital bonding is needed for many efforts to control the chemical reactivity and physical properties of lanthanide compounds. Although ionic bonding dominates most bulk lanthanide properties, some studies suggest that small amounts of covalency have an important impact on the electronic structure and magnetic properties. For example, covalent bonding with the 4f orbitals is an important component of many electronic structure descriptions for formally tetravalent cerium compounds including cerocene, $(C_8H_8)_2Ce$,[1–12] and cerium dioxide, CeO_2.[13–25] In the trivalent state, well-defined interactions with the 4f orbitals are less common.[26–37] However, recent theoretical and spectroscopic studies have recognized the importance of 5d-covalency for a broad range of trivalent lanthanide molecules.[36–46] These effects raise many important questions, such as whether accurate theoretical methodology can treat the 4f-electrons simply as part of the core, or whether a more demanding approach should be followed that allows the 4f-electrons to delocalize and participate in bonding.[22–24,47–55] In addition, controlling the ligand field strength and symmetry is one of the more promising avenues to increase the relaxation barriers of single-molecule magnets.[56–75] Clearly, efforts to harness the unique electronic and magnetic properties of lanthanide elements would benefit from more accurate models of 4f and 5d orbital bonding.

In recent years, ligand K-edge X-ray absorption spectroscopy (XAS) has emerged as one of the most effective and versatile methods to quantify the electronic structure and orbital mixing in d- and f-block materials with bonds to light atoms such as carbon and oxygen.[76–80] The technique measures the intensity of the bound-state transitions between ligand 1s orbitals and unoccupied orbitals with a ligand 2p orbital character.[81–84] Previous work has shown that accurate transition intensities can be obtained at the O K-edge (*ca.* 540 eV) by measuring XAS in transmission mode with a scanning transmission X-ray microscope (STXM).[76,77,80] This spectroscopic approach overcomes many of the errors resulting from surface contamination, saturation, and self-absorption effects, which are typically encountered when using traditional detection methods on non-conducting samples. STXM measurements are conducted on micron-scale particles to ensure that

[a]*Department of Chemistry, University of California, Berkeley CA 94720, USA*
[b]*Chemical Sciences Division, Lawrence Berkeley National Laboratory, Berkeley CA 94720, USA. E-mail: sgminasian@lbl.gov*
[c]*Canadian Light Source, Saskatoon, Saskatchewan S7N 2V3, Canada*
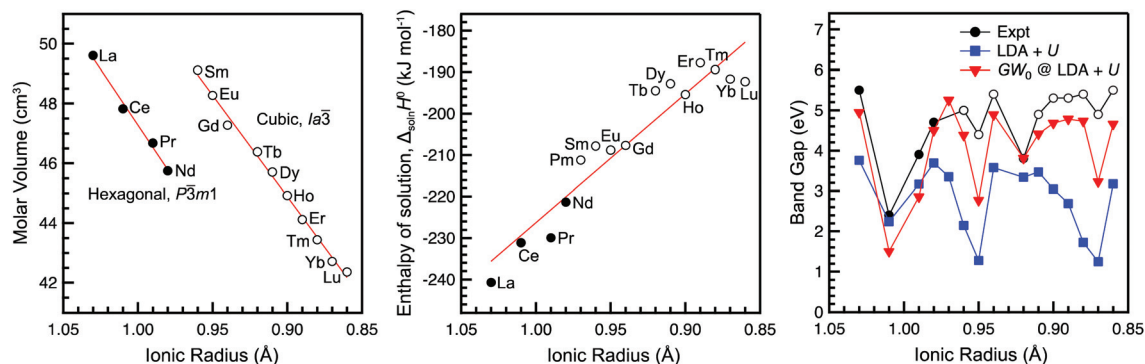†Electronic supplementary information (ESI) available. See DOI: 10.1039/c6dt00358c

Fig. 1 Plots comparing molar volumes (left, representing Ln−O bond distances), enthalpies of solution (middle, representing Ln−O bond energies), and band gaps (right) for the series of lanthanide sesquioxides, Ln_2O_3 (Ln = La to Lu), to the Ln^{3+} ionic radii.[172] For the molar volumes and enthalpies of solution, the approximately linear correlations (red lines) suggest that Ln−O bonding is closely related to the ion sizes. In contrast, periodic variations in the band gaps are not monotonic and suggest that the Ln_2O_3 electronic structure varies across the lanthanide series. (Left) Molar volumes were calculated by multiplying published values[119−130] for the crystallographic volume by the Avogadro constant. (Middle) The enthalpies are calculated as described by Morss and others by using $\Delta_{soln}H^0(LnO_{1.5}) = \Delta_fH^0[M^{3+}(aq)] + 1.5\ \Delta_fH^0[H_2O(l)] - \Delta_fH^0[LnO_{1.5}(s)]$ to correct for the divalent $4f^7 6s^2$ and $4f^{14}6s^2$ ground states of the Eu and Yb metals.[172−174] (Right) Experimental band gaps were determined using optical spectroscopy on single crystals,[90] and calculated band gaps were determined using DFT at the LDA + U and GW_0@LDA + U theory levels.[54] Adapted with permission from H. Jiang, P. Rinke and M. Scheffler, "Electronic properties of lanthanide oxides from the GW perspective," *Phys. Rev. B: Condens. Matter*, 2012, **86**, 125115. Copyright 2012 by the American Physical Society.

the spectral path length is within the linear regime of Beer–Lambert's law, which is particularly advantageous for the examination of the dense solids described below.

In this study, O K-edge XAS from STXM was used to evaluate periodic changes in the electronic structure and orbital mixing for the complete series of lanthanide sesquioxides, Ln_2O_3 (Ln = La to Lu, except radioactive Pm). Ln_2O_3 compounds were chosen because the nature of localized (ionic) and itinerant (covalent) electronic states has a significant impact on their unusual chemical and physical properties.[22,23,54,85−90] In addition to being starting materials for the laboratory-scale synthesis of many other lanthanide materials, lanthanide sesquioxides are irreplaceable components of automotive catalytic converters, lighting phosphors, semiconductors, high-performance electronics, medical technologies, and neutron poisons for nuclear fuel.[89−99] Trivalent Ln_2O_3 compounds can be prepared in high purity for all the lanthanide elements, which provides a unique opportunity to determine how the electronic structure is impacted by changes in 4f and 5d orbital energies and occupancies, symmetry, and coordination number. The sesquioxides also provide a valuable structural comparison for the important but poorly understood transuranic sesquioxides, An_2O_3 (An = Pu, Am, Cm, Bk, and Cf), which do not have an isostructural analog among the lighter actinides such as Th and U. Because the radial extension of the 4f orbitals can be regarded as insufficient to provide overlap with ligand-based orbitals,[50,100−102] most aspects of the Ln_2O_3 structure and bonding are traditionally thought to follow from the monotonic decrease in Ln^{3+} ionic radii observed between La and Lu (Fig. 1). However, recent physical measurements[89,90] and theoretical studies[22,23,54,55,85−88,103] have revealed irregular variations in Ln_2O_3 band gaps (Fig. 1, right), which has far-reaching

consequences for efforts to understand valence orbital composition, mechanisms of conduction, and other physical properties in lanthanide materials.[104−111] The O K-edge XAS results described below provide new insight into this unusual behavior by showing that Ln_2O_3 bonding is far from fully ionic owing to participation of the 5d orbitals.

Results and discussion

Oxygen K-edge measurements and data reduction

All measurements except for Sm_2O_3 were performed with the STXM on the Canadian Light Source (CLS) soft X-ray spectromicroscopy (SM) beamline 10ID-1, which is ideally suited for accurate light atom (C, N, O, F) K-edge XAS measurements on finely divided powders.[112] The O K-edge measurement for Sm_2O_3 was performed using the STXM on Advanced Light Source (ALS) beamline 5.3.2.2.[113] To quantify the absorbance signal, the measured transmitted intensity (I) was converted to optical density using Beer–Lambert's law: $OD = \ln(I/I_0) = \mu\rho d$, where I_0 is the incident photon flux intensity, d is the sample thickness, and μ and ρ are the mass absorption coefficient and density of the sample material, respectively. The Ln_2O_3 compounds are known to crystallize in a variety of highly dense phases,[114−118] such that small, thin particles are needed to avoid saturation effects. For the structure types used in this study (see Experimental), ρ_{calc} increased monotonically from 6.6 to 7.4 g cm^{-1} between La_2O_3 and Nd_2O_3, and from 7.1 to 9.4 between Sm_2O_3 and Lu_2O_3.[119−130] Owing to the challenging nature of STXM measurements on small particles, spectra from multiple particles and beamruns were averaged to achieve the best possible data quality and signal to background ratios.
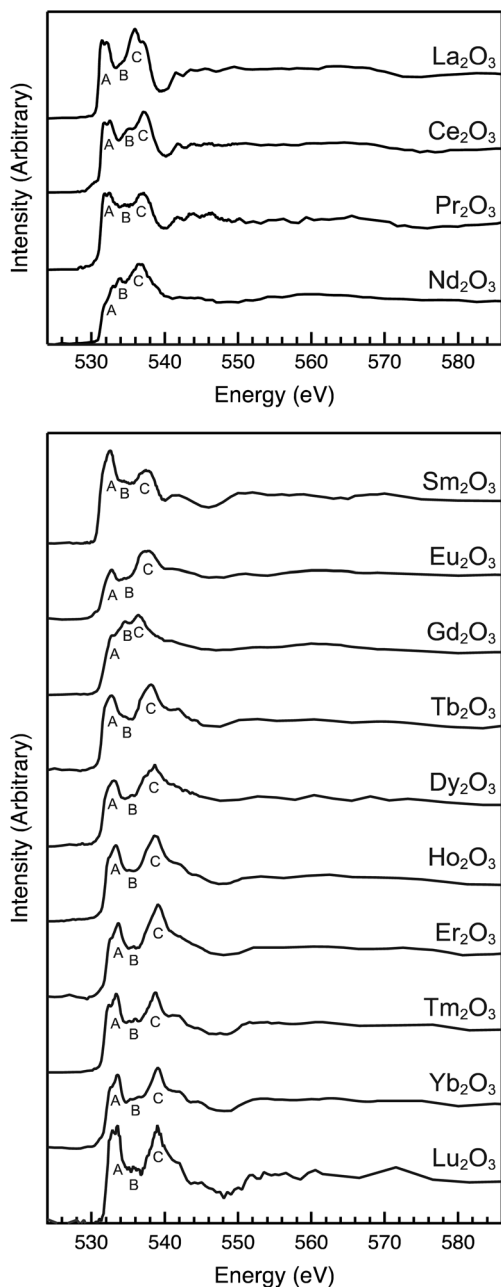
Fig. 2 O K-edge XAS for Ln_2O_3 (Ln = La to Lu). Oxides in the upper and lower panels were prepared in the hexagonal (7-coordinate Ln) and cubic phases (6-coordinate Ln), respectively.

Background-subtracted and normalized O K-edge XAS obtained in transmission using STXM are shown in Fig. 2 for all the Ln_2O_3 compounds from La to Lu (except radioactive Pm). The spectra are similar to those from other O K-edge studies of metal oxides[76,77,80,131–133] in that they exhibit some low energy pre-edge features that – to a first approximation – are indicative of orbital mixing between the O 2p orbitals and lanthanide-based orbitals. With the exception of Nd_2O_3 and Gd_2O_3, each spectrum contains two clearly-resolved bands of transitions: one at low energy centered between 532 and 533 eV

(A-features), and another at high energy centered between 536.5 and 539.5 eV (C-features). Well-resolved features were not always observed in the intermediate region between the two main peaks A and C. However, the spectra did not return to the baseline in this region, which suggests that additional states are present between 533 and 536.5 eV (B-features). The spectra obtained using STXM resemble earlier O K-edge measurements from electron energy-loss spectroscopy (EELS) reported for Ce_2O_3, Gd_2O_3, and Er_2O_3.[134–136] For example, the decreased intensity for the low energy A-features in the Gd_2O_3 spectrum (Fig. 2) is comparable to the results of earlier EELS studies on Gd_2O_3 nanoparticles.[137–139] The STXM data differ in that the high resolving power of the CLS SM beamline (*ca.* 0.1 eV at the O K-edge) reveals the fine structure that was not observed with EELS.

A spectral deconvolution was conducted to quantify changes in peak energy and intensity throughout the Ln_2O_3 series. The O K-edge XAS spectra were modeled as described previously using symmetrically constrained Gaussian line shapes and a step function with a 1:1 ratio of arctangent and error function contributions.[77,78,80] The curve-fitting models are summarized in Table 1 and are shown in Fig. 3. To facilitate spectral interpretations, a complete and self-consistent curve-fitting model accounting for all of the lanthanide oxides was developed and refined by considering changes in all the spectra simultaneously. In each case, the smallest possible number of fit functions was chosen. Hence, the low energy A-features were modeled with two functions (blue). For Ce_2O_3, Eu_2O_3, and Yb_2O_3, an additional, smaller function was added near 530 to 531 eV to account for the small shoulders near the onset of the first bands (orange). The low-intensity valley between the two main bands that includes B-features was modeled with one function (magenta). Finally, the high energy C-features were modeled with two or three functions, depending on the compound (green). In each case, the curve-fits agreed well with experimental data as shown by low values of χ^2, and residual data that deviated little from a straight line of zero intensity. For the A-features, the error in the energy of the corresponding Gaussian functions was less than or equal to the spectroscopic energy resolution of ±0.1 eV. The close proximity of the B- and C-features to each other and to the rising edge resulted in larger errors in the energy of roughly ±0.5 eV.

Transition assignments

Spectral interpretations were formulated within the context of previous spectroscopic[90] and theoretical[54] investigations of Ln_2O_3. Our analysis began with lutetium sesquioxide, Lu_2O_3, because it had a fully occupied $4f^n$ shell (n = 14) and the $4f^{n+1}$ state was inaccessible. Hence, transitions involving the Lu 4f orbitals were ruled out in Lu_2O_3 and O 2p and Ln 4f orbital mixing was initially disregarded (*vide infra*) during O K-edge XAS transition assignments. Within the limits of this model, the peaks observed in the O K-edge XAS of Lu_2O_3 were attributed to the transitions from the O 1s orbitals to unoccupied bands derived from the Lu 5d and 6p orbitals (Fig. 3). Specifically, the low energy A-features were assigned to excitations

Table 1 Oxygen K-edge pre-edge peak energies (eV)[a] and intensities (Int)[b] for Ln$_2$O$_3$ (Ln = La to Lu)

Oxide	Assignment	Energies (eV)	Intensities (Int)
La$_2$O$_3$	A, O 1s → 5d-π	531.3, 532.0	0.5(1), 2.0(2)
	B, O 1s → 6p	533.8	1.8(2)
	C, O 1s → 5d-σ	535.9, 537.5, 538.5	5.8(4)
Ce$_2$O$_3$	A, O 1s → 5d-π	531.6, 532.4	0.4(1), 2.1(2)
	B, O 1s → 6p	534.8	3.6(4)
	C, O 1s → 5d-σ	537.4, 539.3	4.0(3)
Pr$_2$O$_3$	A, O 1s → 5d-π	531.6, 532.2	0.3(1), 1.8(2)
	B, O 1s → 6p	533.9	2.8(3)
	C, O 1s → 5d-σ	537.1, 539.5	5.3(5)
Nd$_2$O$_3$	A, O 1s → 5d-π	531.7, 532.6	0.5(1), 0.3(1)
	B, O 1s → 6p	533.6	2.7(3)
	C, O 1s → 5d-σ	536.4, 539.0	6.8(5)
Sm$_2$O$_3$	A, O 1s → 5d-π	531.4, 532.4	0.7(1), 2.3(2)
	B, O 1s → 6p	534.1	2.8(3)
	C, O 1s → 5d-σ	537.0, 538.5	4.8(5)
Eu$_2$O$_3$	A, O 1s → 5d-π	531.6, 532.6	0.2(1), 1.2(1)
	B, O 1s → 6p	534.5	2.1(2)
	C, O 1s → 5d-σ	536.6, 537.7, 539.2	4.7(3)
Gd$_2$O$_3$	A, O 1s → 5d-π	531.6, 532.6	0.02[c], 1.8(2)
	B, O 1s → 6p	534.4	2.3(2)
	C, O 1s → 5d-σ	536.2, 537.8, 540.2	6.8(5)
Tb$_2$O$_3$	A, O 1s → 5d-π	531.7, 532.6	0.3(1), 2.6(3)
	B, O 1s → 6p	534.6	2.2(2)
	C, O 1s → 5d-σ	536.5, 538.0, 540.8	7.6(5)
Dy$_2$O$_3$	A, O 1s → 5d-π	531.9, 533.0	0.7(1), 2.0(2)
	B, O 1s → 6p	535.2	2.4(2)
	C, O 1s → 5d-σ	536.9, 538.4, 541.3	7.7(5)
Ho$_2$O$_3$	A, O 1s → 5d-π	532.2, 533.2	0.7(1), 2.0(2)
	B, O 1s → 6p	534.9	2.5(3)
	C, O 1s → 5d-σ	538.8, 541.9	8.1(7)
Er$_2$O$_3$	A, O 1s → 5d-π	532.4, 533.5	0.7(1), 1.5(1)
	B, O 1s → 6p	535.1	2.5(3)
	C, O 1s → 5d-σ	539.0, 542.2	8.4(7)
Tm$_2$O$_3$	A, O 1s → 5d-π	532.2, 533.3	1.1(1), 1.8(2)
	B, O 1s → 6p	535.4	2.9(3)
	C, O 1s → 5d-σ	538.7, 541.3	5.7(5)
Yb$_2$O$_3$	A, O 1s → 5d-π	532.4, 533.5	0.8(1), 1.7(2)
	B, O 1s → 6p	535.6	2.8(3)
	C, O 1s → 5d-σ	539.0, 541.6	5.7(5)
Lu$_2$O$_3$	A, O 1s → 5d-π	532.5, 533.5	1.4(1), 1.8(2)
	B, O 1s → 6p	535.3	3.2(3)
	C, O 1s → 5d-σ	539.0, 541.5	6.7(6)

[a] Energies are taken from the position of Gaussian functions used in the curve-fit, and have an estimated error of ±0.1 eV for the two O 1s → 5d-π features and ±0.5 eV for all higher energy features. [b] Intensities are derived from the area under Gaussian functions used in the curve-fit, and have an estimated error of 10%. Intensities of the O 1s → 5d-σ transitions are reported as the sum of all Gaussian functions used in the fit. [c] The 10% error estimation was not given for this feature, which has very little intensity. Intensities between 0.02 and 0.2 were observed after applying larger changes to the overall fit.

from O 1s orbitals to the unoccupied bands resulting from Lu 5d and O 2p π-bonds, while the higher energy C-features were assigned to the excitations from O 1s orbitals to unoccupied bands resulting from Lu 5d and O 2p σ-type bonds. The B-features were assigned to transitions from the O 1s orbitals to bands that are principally derived from the O 2p and Lu 6p orbitals.

Based on this interpretation for Lu$_2$O$_3$, features observed for all the remaining 6- and 7-coordinate Ln$_2$O$_3$ compounds were attributed in the same manner to O 1s transitions into
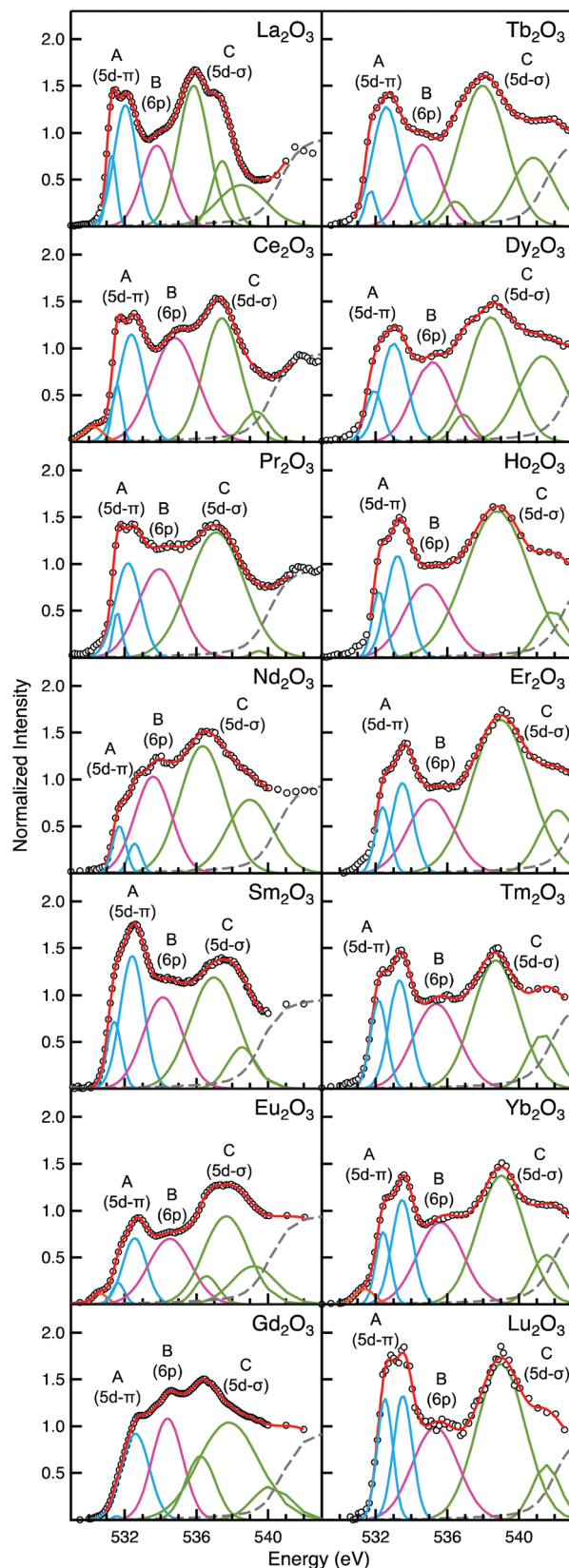
Fig. 3 Oxygen K-edge XAS pre-edges (black circles), Gaussian functions (blue, magenta, green), and step functions (dashed gray) used to generate the curve-fits (red) for particles of Ln$_2$O$_3$ (Ln = La to Lu).

Ln 5d and O 2p π-bands (A-features), Ln 6p and O 2p σ- and π-bands (B-features), and Ln 5d and O 2p σ-bands (C-features), as shown in Fig. 3. There are some inherent shortcomings to this approach, which limits the number of Gaussian functions to model spectra that are likely comprised of hundreds of bound-state transitions. For example, the need for multiple Gaussian functions to model the A- and C-features may derive from differences in the coordination number and geometry, multi-electron effects, and band effects. However, previous experience with other transition metal, lanthanide, and actinide compounds suggested that these effects would not invalidate the very general transition assignments provided above.[46,79,140,141]

These O 1s → 5d transition assignments are consistent with several O K-edge EELS studies on Ce_2O_3 and Er_2O_3,[134,136,142] which also attributed the A and C-features centered at 532.2 and 537.7 eV to transitions involving the Ln 5d π- and σ-bands, respectively. The O 1s → 5d transition assignments for Ce_2O_3 are also supported by reports of the O K-edge XAS of formally tetravalent CeO_2, which provided O 1s → 5d-π (e_g) and O 1s → 5d-σ (t_{2g}) transition energies of 533.5 and 537.9 eV, respectively.[143] We note that recent Cl K-edge XAS and DFT studies have also shown that the 5d orbitals in $CeCl_6{}^{2-}$ and $CeCl_6{}^{3-}$ differ in energy by about 0.5 eV.[46] In addition, studies of the electron density distribution in Ln_2O_3 (Ln = Y, Dy, Ho, Tm, Yb) from synchrotron X-ray diffraction show that, while the majority of 4f electron density is localized, invoking some 5d and 6p orbital involvement in bonding is necessary to explain the overlapping electron clouds for adjacent Ln and O atoms.[129,144]

The O 1s → 6p transition assignments provided in Fig. 3 are consistent with recent CASTEP calculations on Y_2O_3 and La_2O_3, which showed O 2p and Y/La 6p density in the middle of the 5d bands.[88] However, we note that this explanation is at odds with some earlier work. Specifically, O K-edge XAS and theory studies of Y_2O_3 partially reversed this assignment, attributing the B- and C-features to O 1s → 5d-σ and O 1s → 6p transitions, respectively.[145,146] The assignments in Fig. 3 also partially contradict an earlier O K-edge EELS study of Ce_2O_3 by Mullins and coworkers,[134] which attributed the B-features to O 1s → 4f transitions on the basis of XPS measurements.[134,147,148] However, in the case of Lu_2O_3 – which has a fully occupied $4f^{14}$ shell – the O 1s → 4f transition cannot occur and thus the B-features observed in this spectrum were assigned to O 1s → 6p transitions. Clearly, the origin of the B-features in the O K-edge XAS of Ln_2O_3 is complex and likely derives from many unique transitions. Additional experiments and theory are needed to provide a definitive assignment.

The interpretation given above is supported by Fig. 4, which plots the O K-edge transition energies for each of the Ln_2O_3 compounds. Previous work has shown that ligand K-edge transition energies are closely related to the parent metal d or f orbital energies for a structurally-related series of molecules.[46,77–79,82,141] In general, there was a overall increase of 1–2 eV in O K-edge transition energies between La_2O_3 and Lu_2O_3, which is consistent with the slight increase in 5d
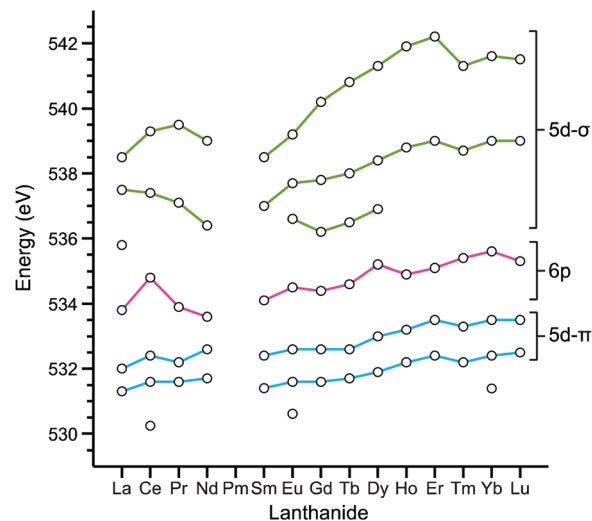

Fig. 4 Plot of the O K-edge transition energies (eV) for Ln_2O_3 from Ln = La to Lu.
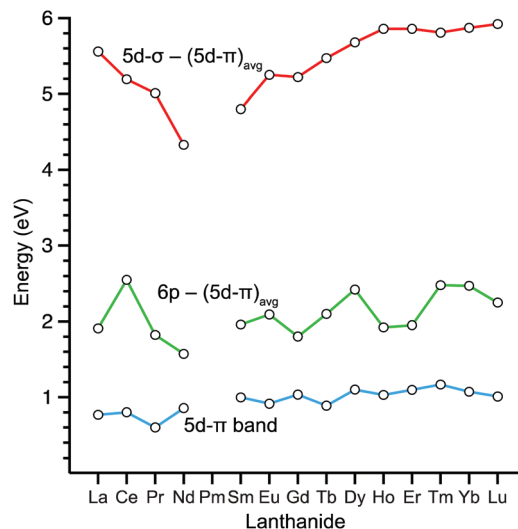

Fig. 5 Plot of the difference in energies between the transitions observed in the O K-edge XAS for Ln_2O_3 (Ln = La to Lu). The 5d-π band splitting is determined from the two Gaussian functions used to model the low energy A-features. $(5d-π)_{avg}$ is equal to the average energy of both low energy functions, weighted by their intensities. Values for the energy of 5d-σ were taken from the most intense function used to model the C-features.

orbital energies that is expected with increasing effective nuclear charge and screening by 4f electrons.[149] The average O 1s → 5d-π transition energies between Ce_2O_3 (532.2 eV) and Gd_2O_3 (532.6 eV) are also consistent with recent Cl K-edge XAS and time-dependent DFT studies on trivalent $LnCl_6{}^{3-}$ compounds (Ln = Ce, Pr, Nd, Pm, Sm, Eu, Gd) that showed only slight changes in Cl 1s → t_{2g} (5d-π) transition energies.[46]

Fig. 5 plots differences in the transition energies, which can be used to compare the relative energies of unoccupied

bands in the Ln_2O_3 compounds. For example, the splitting between A- and C-features was used to estimate the strength of the ligand field imposed on the Ln 5d orbitals by the oxygen atoms, and varied from 4–6 eV for all of the Ln_2O_3. The A–C splittings decreased steadily from La_2O_3 (5.6 eV) to Nd_2O_3 (4.3 eV), and then increased from Sm_2O_3 (4.8 eV) to Ho_2O_3 (5.9 eV) where they remained invariant for the remaining Ln_2O_3. These observations agreed well with the 5.2 to 5.6 eV splittings that were observed in previous O K-edge EELS studies of Ce_2O_3 and Yb_2O_3.[134–136] The experimental values are also in accordance with previous theoretical studies on the Ln_2O_3 compounds, which showed that the distribution of the unoccupied 5d density of states varied from 4 to 6 eV, depending on the functional and code used.[24,51,87,88,142] The two Gaussian functions used to model the A-features (both O 1s → 5d-π) were separated by *ca.* 1 eV for all Ln_2O_3 compounds; new band structure calculations are needed to understand the origin of this splitting.

Spectral intensities

From the spectra shown in Fig. 3, it is clear that there are large differences in the amount of O 2p mixing for different Ln_2O_3. Quantitative trends in the extent of Ln–O orbital mixing can be determined from the intensity (defined as area, see Experimental) of the Gaussian functions used in the curve-fit. Changes in intensity for the A, B, and C features are summarized in Fig. 6 and Table 1. Errors in the spectral intensities for individual Gaussian functions were estimated at 10% based on data reproducibility and observations from earlier O K-edge STXM studies.[77,80] Due to the close proximity to each other and the rising edge, Gaussian functions used to model the high energy B- and C-features were affected by subtle changes

in the curve-fitting model. Because the intensities of these individual Gaussian functions may be less reliable, only the sum of the intensities over a set of features (A, B, or C) is used to draw quantitative conclusions in the following discussion. Fig. 6 also shows the total intensity of all the Gaussian functions, which demonstrates that many of the systematic trends described below are not dependent on the curve-fitting model.

With these considerations in mind, some quantitative changes in O 2p mixing with Ln based orbitals can be identified. Our curve-fitting model suggested that the total intensities of the A-features were statistically equivalent for most of the Ln_2O_3 compounds, averaging 2.3(6). Although a smaller value of 0.8(1) was found for Nd_2O_3, these results suggested that Ln–O π-bonding between the Ln 5d and O 2p orbitals was essentially unchanged for most of the Ln_2O_3 compounds. Much larger changes in the B-feature intensities were observed when moving from left to right in the lanthanide series. For example, the intensities decreased for the 7-coordinate Ln_2O_3 from 3.6(4) (Ce_2O_3) to 2.8(3) (Sm_2O_3), before rising again with the 6-coordinate Ln_2O_3 from 2.1(2) (Eu_2O_3) to 3.2(3) (Lu_2O_3). These results reflect a more pronounced difference in the composition of the Ln–O bonds, such that the amount of O 2p and Ln 6p orbital mixing near the structural change from 7- to 6-coordinate (*e.g.*, Sm_2O_3 and Eu_2O_3) was significantly less than that observed for the analogs at the ends of the series (*e.g.*, Ce_2O_3 and Lu_2O_3). This change may reflect improvements in the spatial overlap with the especially diffuse 6p orbitals, which are more likely to be influenced by changes in bond length, coordination number, and geometry.

In general, the total intensity of the high energy C-features (O 1s → 5d-σ) was 2 to 3 times larger than the total intensity of the A-features (O 1s → 5d-π) and the B-features (O 1s → Ln 6p), which can be attributed to the improved spatial overlap in σ-bonds involving O 2p and Ln 5d orbitals. Surprisingly, the trend in O 2p and Ln 5d σ-bonding is not monotonic. A large increase in the O 1s → 5d-σ intensity was observed for the lighter Ln_2O_3 from 4.0(3) (Ce_2O_3) to 6.8(5) (Nd_2O_3). For the heavier Ln_2O_3, a jump in the intensity was observed from 4.7(3) (Eu_2O_3) to 6.8(5) (Gd_2O_3), which was followed by a sudden drop from 8.4(7) (Er_2O_3) to 5.7(5) (Tm_2O_3). These changes are difficult to rationalize simply on the basis of periodic differences in structure and ion size. However, a strong foundation for these differences in O 2p and Ln 5d σ-bonding was found in several earlier studies on the electronic structure in Ln_2O_3 compounds, which are described below.

Systematic trends in Ln–O bonding

Before beginning discussions on the Ln_2O_3 XAS intensities, some discussions of the earlier studies of the electronic structure in Ln_2O_3 compounds is required. Through high-temperature conductivity experiments,[89] optical spectroscopy,[90] and DFT calculations using the local-density approximation (LDA)[54,55,103] a detailed picture of the Ln_2O_3 electronic structure has emerged which shows that the relative position of the Ln 4f orbitals with respect to the O 2p and 5d orbitals can have a significant effect on the spectroscopic and physical
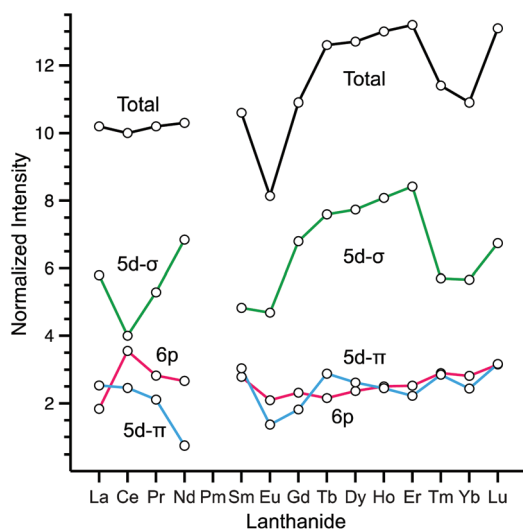

Fig. 6 Comparison of the O K-edge XAS intensity of Gaussian functions comprising the total curve-fit model (black) and separately of the A (O 1s → 5d-π, blue), B (O 1s → 6p, magenta), and C (O 1s → 5d-σ, green) features.
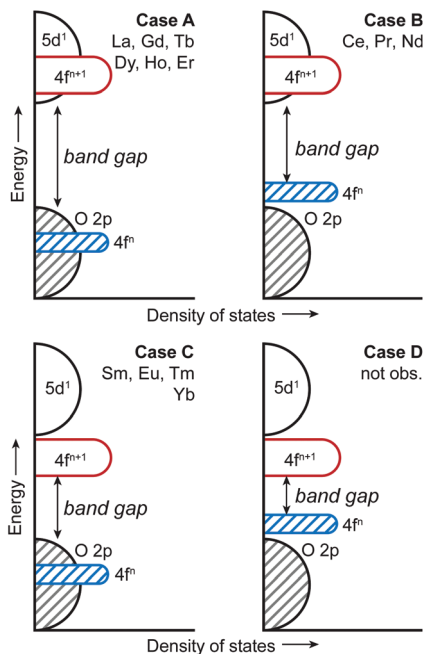
Fig. 7 Qualitative energy band diagrams showing the position of the occupied ($4f^n$) and unoccupied 4f states ($4f^{n+1}$) relative to stationary O 2p (O^{2-}) and $5d^1$ states for Ln_2O_3.
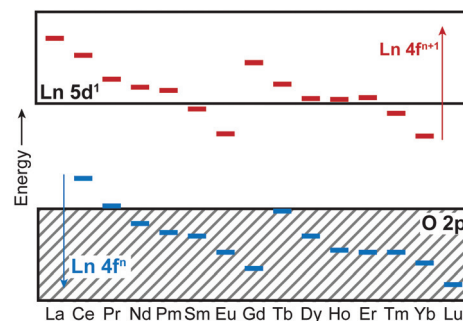

Fig. 8 Qualitative diagram showing how changes in Ln_2O_3 band gaps are driven by periodic variations in the $4f^n$ and $4f^{n+1}$ states relative to the filled O 2p and $5d^1$ states. Energies of the $4f^n$ and $4f^{n+1}$ states are given as $-IP_4$ and $-IP_3$, where IP_3 and IP_4 are the third and fourth ionization potentials, respectively.[151]

properties of Ln_2O_3 compounds. Rather than exhibiting monotonic changes in the electronic structure when moving from left to right in the periodic table, these studies showed that each Ln_2O_3 compound should be categorized by one of four possible "cases" as defined by Lal and Gaur (Fig. 7).[89] In Case A – which includes La, Gd, Tb, Dy, Ho, and Er – the $4f^n$ and $4f^{n+1}$ states are outside of the O 2p–Ln 5d band gap. In Case B – which includes Ce, Pr, and Nd – the $4f^n$ state is above the O 2p valence band maximum and the band gap is Ln 4f–Ln 5d in nature. The situation is reversed in Case C – which includes Sm, Eu, Tm, and Yb – such that the $4f^{n+1}$ state falls below the energy of the 5d conduction band minimum, and the band gap is of a O 2p–Ln 4f nature. Case D, in which both $4f^n$ and $4f^{n+1}$ are in the O 2p–Ln 5d gap, is not observed for any Ln_2O_3 compound.

To simplify comparisons between the Ln_2O_3 O K-edge XAS and these earlier studies, a configuration interaction (CI) model was developed to describe bonding between the O 2p and Ln 4f and 5d orbitals. Compared with molecular orbital theory, CI is well suited to describe bonding in systems containing f orbitals because it is a multi-electron model. CI also explicitly includes the fully ionic configuration, and 4f-orbital bonding is predominantly ionic. Hence, Ln–O bonding involving the O 2p, 4f, and 5d orbitals was described using the following expression

$$\psi^* = N\left[a\left|4f^n5d^0\right\rangle + b\left|4f^n5d^1\underline{L}\right\rangle + c\left|4f^{n+1}5d^0\underline{L}\right\rangle + d\left|4f^{n-1}5d^1\right\rangle\right]$$

$$(1)$$

where N is the normalization constant and a, b, c, and d are the mixing coefficients. The first configuration, $4f^n5d^0$, corresponds to the trivalent state, or the ionic portion of the Ln–O bond. The second and third configurations, $4f^n5d^1\underline{L}$ and $4f^{n+1}5d^0\underline{L}$, are the covalent portions of the Ln–O bonds where $\underline{L}$ represents a ligand hole resulting from ligand to metal charge transfer. The fourth configuration accounts for 4f-electron delocalization through 4f and 5d orbital hybridization. An advantage of this description is that the energies of the $4f^n$ and $4f^{n+1}$ states relative to the $5d^1$ and filled O 2p states can be calculated[54,103] or – for this analysis – estimated from the second and third ionization potentials and f to d promotion energies,[150] as shown in Fig. 8 and S1 in the ESI.†[151]

Because Ln_2O_3 bonding is predominantly ionic, the $4f^n5d^0$ configuration is the largest contributor to the ground state electronic structure (large a in eqn (1)). However, the large difference between C-feature intensities for Case A, B, and C oxides suggests that significant differences in the amount of O 2p σ-type mixing with the Ln 5d orbitals occurred, even for adjacent Ln_2O_3 compounds.

Interpretations of ligand K-edge XAS trends have frequently relied on first-order perturbation theory,[77,78,141,152] in which orbital mixing is proportional to the spatial overlap and energy match between the atomic orbitals. Because the radial extension of the 4f orbitals is small, increases in 4f orbital covalency have primarily been achieved by minimizing the energy separation (degeneracy driven covalency).[127,138,139] Within the limits of this model, changes in the intensity of the O K-edge can be rationalized using eqn (1) in the following manner:

Case A Ln_2O_3: Ln = La, Gd, Tb, Dy, Ho, Er. There are no $4f^n$ or $4f^{n+1}$ states in the gap between the filled O 2p and Ln $5d^1$ states. As a result, O 2p and Ln 5d-σ orbital mixing is the predominant contributor to the covalent part of the Ln–O bond (large b in eqn (1)), which is reflected by more intense O K-edge transitions, on average, than those observed for the other Ln_2O_3.

Case B Ln_2O_3: Ln = Ce, Pr, Nd. The $4f^n$ states are in the gap between filled O 2p and Ln $5d^1$ states, which increases 4f and 5d orbital hybridization (large d in eqn (1)). This increase in

hybridization offsets O 2p and Ln 5d-σ mixing, leading to weaker O K-edge transition intensities – especially for Ce. However, this effect diminishes rapidly as the $4f^n$ states decrease in energy from Ce to Pr to Nd (Fig. 8), resulting in O 2p–Ln 5d-σ mixing and O K-edge XAS intensities that more closely resemble Case A oxides.

Case C Ln_2O_3: Ln = Sm, Eu, Tm, Yb. The $4f^{n+1}$ states fall within the gap between filled O 2p and Ln $5d^1$ states, which increases O 2p and Ln 4f orbital mixing (large *c* in eqn (1)). As observed for Case B, this increase in O 2p and Ln 4f orbital mixing is offset by a decreasing amount of O 2p and Ln 5d-σ bonding, such that weaker transitions are observed in the O K-edge XAS.

Fig. 9 shows how the spectra can be partitioned into several groups with distinct behavior, and correlates well with expectations from the physical and theoretical studies described above.[54] For example, O 1s → 5d-σ transitions observed for Case A oxides were generally the most intense, rising systematically in energy and intensity with increasing 4f orbital occupancy from 5.8(4) (La_2O_3) to 6.8(5) (Gd_2O_3) to 8.4(7) (Er_2O_3). Ce_2O_3 had the weakest O 1s → 5d-σ transitions of all the Ln_2O_3 (4.0(3)) but the intensity increased rapidly and systematically to 5.3(5) and 6.8(5) for Case B oxides Pr_2O_3 and Nd_2O_3, respectively. Case C oxides had uniformly weaker O 1s → 5d-σ transitions, but also exhibited an increase in the intensity with larger 4f-electron counts. Lu_2O_3 was an outlier in this band model; the nonconformity of Lu_2O_3 has been attributed to the elimination of spin orbit coupling.[54]

From the synthetic chemist's perspective, these observations have important implications for understanding general trends in lanthanide reactivity, redox behavior, magnetism, and electrical conduction. For example, the O K-edge XAS
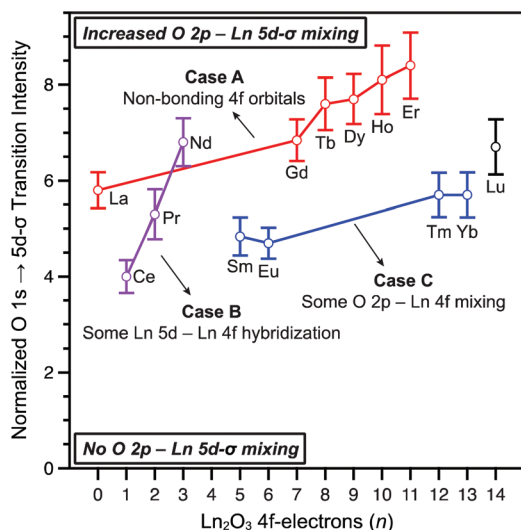

Fig. 9 Plot of the total O 1s → 5d-σ (C features) transition intensities for Ln_2O_3 compounds. The red, blue, and purple lines highlight the correspondence between the systematic increases in O 1s → 5d-σ intensities and well-established differences in the band structure of Ln_2O_3 compounds.[54,89,90,103]

shows that the 4f orbitals in Case A Ln_2O_3 are chemically inactive as either electron donors or acceptors. Hence, Case A lanthanides are most often found in the trivalent ($4f^n$) state, despite having a significant amount of 5d-covalency. According to the lanthanide fourth ionization potentials,[151] the energy of the 4f orbitals decreases when moving from left to right in the periodic table, first from Ce to Gd, and again from Tb to Lu in the second half of the series (Fig. 8). Hence, for Case B lanthanides the 4f orbitals are high in energy and 4f-electron delocalization is enhanced through hybridization with the 5d orbitals. The effect of this is that Case B lanthanides are better electron donors and can access the tetravalent oxidation state more easily. The picture is reversed for Case C oxides, such that Sm, Eu, Tm, and Yb are better electron acceptors and more susceptible to reduction to a divalent Ln^{2+} state ($4f^{n+1}$).

There are some subtleties to the correlation between these O K-edge XAS measurements and earlier work. Firstly, theory, high-temperature conductivity measurements, and optical absorption experiments suggest that monoclinic Tb_2O_3 should be described by a Case B band model.[54,89,90] Cubic Tb_2O_3 was used for the O K-edge XAS measurements, and a Case A band model was invoked. This discrepancy almost certainly reflects differences in the monoclinic and cubic structure types,[117,118,153] because f–d mixing is forbidden in cubic symmetry. One additional curiosity associated with the O K-edge XAS was the presence of small shoulders near the onset of the A-features for Ce_2O_3, Eu_2O_3, and Yb_2O_3. These low energy transitions were much less intense than the primary O 1s → 5d-σ and O 1s → 5d-π transitions, which suggests that they were associated with the final states that had insignificant contributions to the Ln–O bonds. Based on the Case B band model for Eu_2O_3 and Yb_2O_3, it is tempting to suggest that these are transitions to $4f^{n+1}$ states derived from very small amounts of mixing between the O 2p and 4f orbitals. However, analogous features were not resolved for the other Case B oxides Sm_2O_3 and Tm_2O_3. The observation of a similar feature in the spectrum of Ce_2O_3 may reflect trace amounts of CeO_2 contamination, but it is difficult to rule out the possibility of transitions to Rydberg-type orbitals that are commonly seen in ligand K-edge studies.[76,77,132,141,154,155] Additional experiments are needed to validate these interpretations.

Results from this O K-edge XAS study complement recent work from the Evans group, who have synthesized [K(2.2.2-cryptand)][$(C_5H_4SiMe_3)_3Ln$] complexes containing all the Ln^{2+} ions (except Pm),[37,156–158] as well as Th^{2+} and U^{2+}.[159,160] A comprehensive structural, spectroscopic, and theoretical investigation indicated that the Sm^{2+}, Eu^{2+}, Tm^{2+} and Yb^{2+} ions had $4f^{n+1}5d^0$ ground states, while Y^{2+}, La^{2+}, Ce^{2+}, Pr^{2+}, Nd^{2+}, Gd^{2+}, Tb^{2+}, Dy^{2+}, Ho^{2+}, Er^{2+}, and Lu^{2+} all had $4f^n5d^1$ ground states.[37] The [$(C_5H_4SiMe_3)_3Ln$]$^{1-}$ studies also revealed that some lanthanides can cross over between electronic configurations depending on the coordination environment. For example, the ground states of Nd^{2+} and Dy^{2+} were $4f^n5d^1$ in the Evans' organometallic system and $4f^{n+1}5d^0$ in most other solution and solid-state studies of divalent compounds. This behavior is not

unique to the divalent lanthanides, as a related phenomenon was described above for the trivalent Ln^{3+} ions in Ln_2O_3. For example, the O K-edge XAS of cubic, 6-coordinate Tb_2O_3 suggests that O 2p and Ln 5d orbital mixing contributed to a more covalent ground state for Tb^{3+} (Case A, larger b in eqn (1)), while high-temperature conductivity measurements[89] on monoclinic, 7-coordinate Tb_2O_3 indicate that Ln 4f and 5d orbital hybridization led to more 4f-electron itinerancy in the Tb^{3+} ground state (Case B, larger d in eqn (1)). These differences signal a change in the type of orbital mixing that occurs in Tb_2O_3, while maintaining that the ground state in both monoclinic and cubic Tb_2O_3 is likely dominated by the ionic configuration, $4f^n5d^0$. In a strictly qualitative sense, Fig. 8 explains this behavior for Tb_2O_3 by showing that the energies of the $4f^n$ states are almost the same as the top of the filled O 2p states, and suggests that orbital mixing could also vary for other Ln^{3+} ions depending on relative orbital energies (e.g., Pr^{3+}, Nd^{3+}, and Sm^{3+}).[54,89,90,103] These observations provide additional support to the idea that ligand fields can be tuned to vary the physical properties and the accessibility of different redox states for lanthanides and actinides.[35,36,64,69,159,161]

Summary and conclusions

The results presented in this study show that O K-edge XAS provides unique insight that can be used to identify experimental trends in Ln–O bonding for lanthanide oxides. The presence of well-resolved pre-edge transitions provided unambiguous evidence for covalent mixing between the O 2p orbitals and lanthanide-based 5d and 6p orbitals. O K-edge XAS also provided a unique opportunity to quantify changes in the σ and π components of Ln–O bonds independently. For example, a modest and essentially invariant amount of π-type mixing between the Ln 5d and O 2p orbitals was observed for all of the Ln_2O_3 compounds. In contrast, O 2p–Ln 5d σ-type mixing was significant and exhibited multiple abrupt changes that signaled large shifts in the electronic structure. This revealed a complex picture of the electronic structure in Ln_2O_3 that is not obtained from the examination of Ln–O bond lengths and bond strengths, which are largely driven by the monotonic decrease in Ln^{3+} ionic radii from La to Lu.

A simple theoretical framework to rationalize these results was developed around the concept of "degeneracy-driven covalency", where increases in covalency are achieved by decreasing the energy separation between atomic orbitals.[141,162,163] In this model, the set of Ln_2O_3 where Ln = La, Gd, Tb, Dy, Ho, and Er exhibited the most Ln 5d and O 2p orbital mixing, and the covalent part of the Ln–O bond was best described by O 2p → 5d charge transfer. The Ln 4f and 5d orbitals were closer in energy for Ce, Pr, and Nd, which increased 4f–5d hybridization and created more accessible pathways to delocalize the 4f-electrons. Moving later in each half of the series towards Sm, Eu and Tm, Yb brought the O 2p and Ln 4f orbitals closer in energy, such that the amount of O 2p → 4f charge transfer increased. These studies suggest that new electronic structure modes and chemical reactivities may be achieved by using ligand design to tune the energies of filled ligand p and lanthanide d orbitals relative to the 4f orbitals. Recent work by the Evans group has proven the utility of this approach by showing that the [K(2.2.2-cryptand)] [$(C_5H_4SiMe_3)_3Ln$] ligand system stabilizes the $4f^n5d^1$ ground state for Dy^{2+} and Nd^{2+} ions, which were described by $4f^{n+1}5d^0$ electronic configurations for other solution and solid-state compounds.[37,164] Additional studies comparing the same oxide composition in different phases (e.g., cubic vs. hexagonal Tb_2O_3) are underway to evaluate the role of coordination geometries and orbital overlaps while keeping the parent atomic orbital energies constant.

From a technical standpoint, the approach used in this study shows that conducting transmission XAS measurements on micron-scale particles using STXM overcomes many of the inherent difficulties associated with obtaining accurate O K-edge XAS on dense oxide materials. Interpreting the Ln_2O_3 spectra also posed unique challenges derived from the low-symmetry coordination environments, open-shelled electronic configurations, and interactions with multiple 4f, 5d, and 6p orbitals. In this study, comparisons were developed for a complete series of Ln_2O_3 (except radioactive Pm), which provided a sound basis for validating data reduction schemes and spectral interpretations. Additional experiments are needed to determine if this approach can be applied to systems with different ligands, or with different metals and orbital energies. Along these lines, future work will include the transuranic sesquioxides An_2O_3 (An = Pu, Am, Cm, Bk, and Cf), where chemical bonding with both the 5f and 6d orbitals is anticipated to result in increasingly complex spectra.

Experimental

Sample preparation

For this study, La_2O_3, Ce_2O_3, Pr_2O_3 and Nd_2O_3 were prepared in the hexagonal, $P\bar{3}m1$ phase, and the remaining oxides were prepared in the cubic, $Ia\bar{3}$ phase. With some exceptions described below, the lanthanide sesquioxides were obtained from commercial sources, dried at 150 °C under vacuum of 10^{-5} torr for 24 h, and used without further purification. La_2O_3 was prepared by calcination of $La(OH)_3$ in air at 1100 °C for 24 h. Canary yellow Ce_2O_3 was prepared by the reduction of CeO_2 with pure H_2 gas in a Ta boat at 1150 °C for 24 h.[165] Green Pr_2O_3 was prepared by the reduction of Pr_6O_{11} under vacuum (4×10^{-6} torr) at 1100 °C.[166] Sm_2O_3 was prepared by heating $Sm(NO_3)_3(H_2O)_6$ in air to 700 °C for 12 h.[116] White Tb_2O_3 was prepared by reduction of the oxalate with H_2 gas at 650 °C.[167] All the lanthanide sesquioxides were characterized using powder X-ray diffraction to confirm the composition and phase purity. To ensure that samples did not contain adventitious oxygen, all manipulations were performed with rigorous exclusion of air and moisture in a glovebox under an argon atmosphere. Samples were prepared as described previously[77,80,168,169] by brushing the fine powder onto a Si_3N_4

membrane (100 nm, Silson) with a small fiber. A second membrane was placed over the sample, and the edges were sealed together using Hardman Double/Bubble 5-minute epoxy.

Oxygen K-edge measurements

STXM methodology was similar to that discussed previously.[77,80,168,169] Single-energy images and O K-edge XAS spectra were acquired using the STXM instrument at the Canadian Light Source (CLS) spectromicroscopy beamline 10ID-1, which is operated in decay mode (250 to 150 mA, in a *ca.* 0.5 atm He-filled chamber). The beamline uses photons from an elliptically polarizing undulator that delivers photons in the 130 to 2700 eV energy range to an entrance slit-less plane-grating monochromator.[112] The beamline energy was calibrated to a Rydberg feature at the O K-edge for CO_2 gas (538.9 eV). The maximum energy resolution $E/\Delta E$ was previously determined to be better than 7500,[112] which is consistent with the observed standard deviation for spectral transitions of ±0.1 eV determined from the comparison of spectral features over multiple particles and beam runs. For these measurements, the X-ray beam was focused with a zone plate onto the sample, and the transmitted light was detected. The spot size and spectral resolution were determined from the characteristics of the 35 nm zone plate. Images at a single energy were obtained by raster-scanning the sample and collecting transmitted monochromatic light as a function of the sample position. Spectra at particular regions of interest on the sample image were extracted from the "stack", which is a collection of images recorded at multiple, closely spaced photon energies across the absorption edge. Dwell times used to acquire an image at a single photon energy were 2 ms per pixel and spectra were obtained using circularly polarized radiation.

The incident beam intensity was measured through the sample-free region of the Si_3N_4 windows. In order to ensure that the spectra were in the linear regime of Beer–Lambert's law, particles with an absorption of less than 1.5 OD were used. Because lanthanide sesquioxides are strongly absorbing materials with densities ranging from 6 to 9 g mL^{-1}, and because oxygen has a large X-ray absorption cross-section, small particles were selected with lengths of the order of 100 nm in a given dimension. Particles were homogeneous and did not show signs of radiation damage following data acquisition. High quality spectra were obtained by averaging measurements from multiple independent particles, samples, and beam runs.

Data analysis

The O K-edge STXM data were background subtracted using the MBACK algorithm in MATLAB and by setting the edge jump at 541 eV to an intensity of 1.0.[170] Fits to the O K-edges were performed using the program IGOR 6.0 and a modified version of EDG_FIT.[171] Second-derivative spectra were used as guides to determine the number and position of peaks. Pre-edge and rising edge features were modeled a Gaussian line shapes and a step function. For the step function, a 1:1 ratio

of arctangent and error function contributions was employed. Fits were performed over several energy ranges. The quality of each curve fit was determined by evaluating changes in the χ^2 and by inspecting the residual intensity, which is obtained by subtracting the fit from the experiment and should resemble a horizontal line at zero. The area under the pre-edge peaks (defined as the intensity) was calculated with the formula fwhm × ph × $(1/2)(\pi/\ln 2)^{1/2}$, where fwhm = full width at half maximum height (eV), ph = peak height (normalized intensity), and the value $(1/2)(\pi/\ln 2)^{1/2} \approx 1.065$ is a constant associated with the Gaussian function.

For the heavier Ln_2O_3 (Ln = Ho to Lu), fully unconstrained models did not converge with realistic parameters for the width of the functions used to model the poorly-resolved B-features. As discussed in other recent ligand K-edge studies using STXM,[78] reasonable parameter constraints can help to obtain relevant and worthwhile models of the spectra that have high statistical noise. To obtain reasonable models and avoid excessively broad functions, the peak height to peak width ratios for the main functions were constrained to 0.25 (Int per eV) or greater, based on the observations from other O K-edge studies.[77]

Acknowledgements

References

1 F. Mares, K. Hodgson and A. Streitwieser, *J. Organomet. Chem.*, 1970, **24**, C68–C70.

2 A. Greco, S. Cesca and G. Bertolini, *J. Organomet. Chem.*, 1976, **113**, 321–330.

3 P. N. Hazin, J. W. Bruno and H. G. Brittain, *Organometallics*, 1987, **6**, 913–918.

4   M. Dolg, P. Fulde, W. Kuchle, C. S. Neumann and H. Stoll, *J. Chem. Phys.*, 1991, **94**, 3011–3017.

5   M. Dolg, P. Fulde, H. Stoll, H. Preuss, A. Chang and R. M. Pitzer, *Chem. Phys.*, 1995, **195**, 71–82.

6   N. Kaltsoyannis and B. E. Bursten, *J. Organomet. Chem.*, 1997, **528**, 19–33.

7   C. H. Booth, M. D. Walter, M. Daniel, W. W. Lukens and R. A. Andersen, *Phys. Rev. Lett.*, 2005, **95**, 267202.

8   M. D. Walter, C. H. Booth, W. W. Lukens and R. A. Andersen, *Organometallics*, 2009, **28**, 698–707.

9   A. Kerridge, R. Coates and N. Kaltsoyannis, *J. Phys. Chem. A*, 2009, **113**, 2896–2905.

10 A. Kerridge, *Dalton Trans.*, 2013, **42**, 16428–16436.

11 O. Moossen and M. Dolg, *Chem. Phys. Lett.*, 2014, **594**, 47–50.

12 J. J. Le Roy, I. Korobkov, J. E. Kim, E. J. Schelter and M. Murugesu, *Dalton Trans.*, 2014, **43**, 2737–2740.

13 G. Kaindl, G. Kalkowski, W. D. Brewer, B. Perscheid and F. Holtzberg, *J. Appl. Phys.*, 1984, **55**, 1910–1915.

14 B. T. Thole, G. Vanderlaan, J. C. Fuggle, G. A. Sawatzky, R. C. Karnatak and J. M. Esteva, *Phys. Rev. B: Condens. Matter*, 1985, **32**, 5107–5118.

15 A. Bianconi, A. Marcelli, H. Dexpert, R. Karnatak, A. Kotani, T. Jo and J. Petiau, *Phys. Rev. B: Condens. Matter*, 1987, **35**, 806–812.

16 H. Dexpert, R. C. Karnatak, J. M. Esteva, J. P. Connerade, M. Gasgnier, P. E. Caro and L. Albert, *Phys. Rev. B: Condens. Matter*, 1987, **36**, 1750–1753.

17 G. Kaindl, G. Schmiester, E. V. Sampathkumaran and P. Wachter, *Phys. Rev. B: Condens. Matter*, 1988, **38**, 10174–10177.

18 T. Jo and A. Kotani, *Phys. Rev. B: Condens. Matter*, 1988, **38**, 830–833.

19 A. Kotani and H. Ogasawara, *J. Electron Spectrosc. Relat. Phenom.*, 1992, **60**, 257–299.

20 R. C. Karnatak, *J. Alloys Compd.*, 1993, **192**, 64–68.

21 Z. Hu, G. Kaindl, H. Ogasawara, A. Kotani and I. Felner, *Chem. Phys. Lett.*, 2000, **325**, 241–250.

22 P. J. Hay, R. L. Martin, J. Uddin and G. E. Scuseria, *J. Chem. Phys.*, 2006, **125**, 034712.

23 J. L. F. Da Silva, M. V. Ganduglia-Pirovano, J. Sauer, V. Bayer and G. Kresse, *Phys. Rev. B: Condens. Matter*, 2007, **75**, 045121.

24 D. A. Andersson, S. I. Simak, B. Johansson, I. A. Abrikosov and N. V. Skorodumova, *Phys. Rev. B: Condens. Matter*, 2007, **75**, 035109.

25 A. Kotani, *Mod. Phys. Lett. B*, 2013, **27**, 1330012.

26 D. M. Anderson, F. G. N. Cloke, P. A. Cox, N. Edelstein, J. C. Green, T. Pang, A. A. Sameh and G. Shalimoff, *J. Chem. Soc., Chem. Commun.*, 1989, 53–55.

27 W. A. King, T. J. Marks, D. M. Anderson, D. J. Duncalf and F. G. N. Cloke, *J. Am. Chem. Soc.*, 1992, **114**, 9221–9223.

28 C. H. Booth, D. Kazhdan, E. L. Werkema, M. D. Walter, W. W. Lukens, E. D. Bauer, Y.-J. Hu, L. Maron, O. Eisenstein, M. Head-Gordon and R. A. Andersen, *J. Am. Chem. Soc.*, 2010, **132**, 17537–17549.

29 E. J. Schelter, R. Wu, J. M. Veauthier, E. D. Bauer, C. H. Booth, R. K. Thomson, C. R. Graves, K. D. John, B. L. Scott, J. D. Thompson, D. E. Morris and J. L. Kiplinger, *Inorg. Chem.*, 2010, **49**, 1995–2007.

30 M. Coreno, M. de Simone, R. Coates, M. S. Denning, R. G. Denning, J. C. Green, C. Hunston, N. Kaltsoyannis and A. Sella, *Organometallics*, 2010, **29**, 4752–4755.

31 R. G. Denning, J. Harmer, J. C. Green and M. Irwin, *J. Am. Chem. Soc.*, 2011, **133**, 20644–20660.

32 W. W. Lukens, N. Magnani and C. H. Booth, *Inorg. Chem.*, 2012, **51**, 10105–10110.

33 J. R. Robinson, Z. Gordon, C. H. Booth, P. J. Carroll, P. J. Walsh and E. J. Schelter, *J. Am. Chem. Soc.*, 2013, **135**, 19016–19024.

34 J. A. Bogart, A. J. Lewis, S. A. Medling, N. A. Piro, P. J. Carroll, C. H. Booth and E. J. Schelter, *Inorg. Chem.*, 2013, **52**, 11600–11607.

35 J. A. Bogart, A. J. Lewis, M. A. Boreen, H. B. Lee, S. A. Medling, P. J. Carroll, C. H. Booth and E. J. Schelter, *Inorg. Chem.*, 2015, **54**, 2830–2837.

36 J. F. Corbey, D. H. Woen, C. T. Palumbo, M. E. Fieser, J. W. Ziller, F. Furche and W. J. Evans, *Organometallics*, 2015, **34**, 3909–3921.

37 M. E. Fieser, M. R. MacDonald, B. T. Krull, J. E. Bates, J. W. Ziller, F. Furche and W. J. Evans, *J. Am. Chem. Soc.*, 2015, **137**, 369–382.

38 P. Selg, H. H. Brintzinger, M. Schultz and R. A. Andersen, *Organometallics*, 2002, **21**, 3100–3107.

39 G. R. Giesbrecht, J. C. Gordon, D. L. Clark, P. J. Hay, B. L. Scott and C. D. Tait, *J. Am. Chem. Soc.*, 2004, **126**, 6387–6401.

40 J. C. Gordon, G. R. Giesbrecht, D. L. Clark, P. J. Hay, D. W. Keogh, R. Poli, B. L. Scott and J. G. Watkin, *Organometallics*, 2002, **21**, 4726–4734.

41 P. L. Arnold, S. T. Liddle, J. McMaster, C. Jones and D. P. Mills, *J. Am. Chem. Soc.*, 2007, **129**, 5360–5361.

42 S. G. Minasian, J. L. Krinsky, J. D. Rinehart, R. Copping, T. Tyliszczak, M. Janousch, D. K. Shuh and J. Arnold, *J. Am. Chem. Soc.*, 2009, **131**, 13767–13783.

43 P. L. Arnold, Z. R. Turner, N. Kaltsoyannis, P. Pelekanaki, R. M. Bellabarba and R. P. Tooze, *Chem. – Eur. J.*, 2010, **16**, 9623–9629.

44 J. L. Krinsky, S. G. Minasian and J. Arnold, *Inorg. Chem.*, 2011, **50**, 345–357.

45 G. Nocton, W. W. Lukens, C. H. Booth, S. S. Rozenel, S. A. Medling, L. Maron and R. A. Andersen, *J. Am. Chem. Soc.*, 2014, **136**, 8626–8641.

46 M. W. Löble, J. M. Keith, A. B. Altman, S. C. E. Stieber, E. R. Batista, K. S. Boland, S. D. Conradson, D. L. Clark, J. Lezama Pacheco, S. A. Kozimor, R. L. Martin, S. G. Minasian, A. C. Olson, B. L. Scott, D. K. Shuh, T. Tyliszczak, M. P. Wilkerson and R. A. Zehnder, *J. Am. Chem. Soc.*, 2015, **137**, 2506–2523.

47 P. Strange, A. Svane, W. M. Temmerman, Z. Szotek and H. Winter, *Nature*, 1999, **399**, 756–758.

48 A. Svane, W. M. Temmerman, Z. Szotek, L. Petit, P. Strange and H. Winter, *Phys. Rev. B: Condens. Matter*, 2000, **62**, 13394–13399.

49 L. Petit, A. Svane, Z. Szotek, P. Strange, H. Winter and W. M. Temmerman, *J. Phys.: Condens. Matter*, 2001, **13**, 8697–8706.

50 M. Atanasov, C. Daul, H. U. Gudel, T. A. Wesolowski and M. Zbiri, *Inorg. Chem.*, 2005, **44**, 2954–2963.

51 C. Loschen, J. Carrasco, K. M. Neyman and F. Illas, *Phys. Rev. B: Condens. Matter*, 2007, **75**, 035115.

52 H. Jiang, R. I. Gomez-Abal, P. Rinke and M. Scheffler, *Phys. Rev. Lett.*, 2009, **102**, 126403.

53 J. Kullgren, C. W. M. Castleton, C. Muller, D. M. Ramo and K. Hermansson, *J. Chem. Phys.*, 2010, **132**, 054110.

54 H. Jiang, P. Rinke and M. Scheffler, *Phys. Rev. B: Condens. Matter*, 2012, **86**, 125115.

55 R. Gillen, S. J. Clark and J. Robertson, *Phys. Rev. B: Condens. Matter*, 2013, **87**, 125116.

56 R. Sessoli and A. K. Powell, *Coord. Chem. Rev.*, 2009, **253**, 2328–2341.

57 J. D. Rinehart and J. R. Long, *Chem. Sci.*, 2011, **2**, 2078–2085.

58 J. J. Baldovi, S. Cardona-Serra, J. M. Clemente-Juan, E. Coronado, A. Gaita-Arino and A. Palii, *Inorg. Chem.*, 2012, **51**, 12565–12574.

59 F. Tuna, C. A. Smith, M. Bodensteiner, L. Ungur, L. F. Chibotaru, E. J. L. McInnes, R. E. P. Winpenny, D. Collison and R. A. Layfield, *Angew. Chem., Int. Ed.*, 2012, **51**, 6976–6980.

60 S. Demir, J. M. Zadrozny, M. Nippe and J. R. Long, *J. Am. Chem. Soc.*, 2012, **134**, 18546–18549.

61 R. J. Blagg, L. Ungur, F. Tuna, J. Speak, P. Comar, D. Collison, W. Wernsdorfer, E. J. L. McInnes, L. F. Chibotaru and R. E. P. Winpenny, *Nat. Chem.*, 2013, **5**, 673–678.

62 D. N. Woodruff, R. E. P. Winpenny and R. A. Layfield, *Chem. Rev.*, 2013, **113**, 5110–5148.

63 L. Ungur, J. J. Le Roy, I. Korobkov, M. Murugesu and L. F. Chibotaru, *Angew. Chem., Int. Ed.*, 2014, **53**, 4413–4417.

64 K. R. Meihaus, J. F. Corbey, M. Fang, J. W. Ziller, J. R. Long and W. J. Evans, *Inorg. Chem.*, 2014, **53**, 3099–3107.

65 J. J. Baldovi, J. M. Clemente-Juan, E. Coronado, Y. Duan, A. Gaita-Arino and C. Gimenez-Saiz, *Inorg. Chem.*, 2014, **53**, 9976–9980.

66 S. K. Singh, T. Gupta, M. Shanmugam and G. Rajaraman, *Chem. Commun.*, 2014, **50**, 15513–15516.

67 W. Huang, J. J. Le Roy, S. I. Khan, L. Ungur, M. Murugesu and P. L. Diaconescu, *Inorg. Chem.*, 2015, **54**, 2374–2382.

68 S. Demir, I.-R. Jeon, J. R. Long and T. D. Harris, *Coord. Chem. Rev.*, 2015, **289**, 149–176.

69 K. R. Meihaus, M. E. Fieser, J. F. Corbey, W. J. Evans and J. R. Long, *J. Am. Chem. Soc.*, 2015, **137**, 9855–9860.

70 A. J. Brown, D. Pinkowicz, M. R. Saber and K. R. Dunbar, *Angew. Chem., Int. Ed.*, 2015, **54**, 5864–5868.

71 N. F. Chilton, *Inorg. Chem.*, 2015, **54**, 2097–2099.

72 W. Huang, J. Xu, D. Wu, X. Huang and J. Jiang, *New J. Chem.*, 2015, **39**, 8650–8657.

73 X.-L. Li, H. Li, D.-M. Chen, C. Wang, J. Wu, J. Tang, W. Shi and P. Cheng, *Dalton Trans.*, 2015, **44**, 20316–20320.

74 K. Liu, H. Li, X. Zhang, W. Shi and P. Cheng, *Inorg. Chem.*, 2015, **54**, 10224–10231.

75 A. A. Trifonov, B. Shestakov, J. Long, K. Lyssenko, Y. Guari and J. Larionova, *Inorg. Chem.*, 2015, **54**, 7667–7669.

76 J. A. Bradley, P. Yang, E. R. Batista, K. S. Boland, C. J. Burns, D. L. Clark, S. D. Conradson, S. A. Kozimor, R. L. Martin, G. T. Seidler, B. L. Scott, D. K. Shuh, T. Tyliszczak, M. P. Wilkerson and L. E. Wolfsberg, *J. Am. Chem. Soc.*, 2010, **132**, 13914–13921.

77 S. G. Minasian, J. M. Keith, E. R. Batista, K. S. Boland, J. A. Bradley, S. R. Daly, D. Sokaras, S. A. Kozimor, W. W. Lukens, R. L. Martin, D. Nordlund, G. T. Seidler, D. K. Shuh, T. Tyliszczak, G. L. Wagner, T. C. Weng and P. Yang, *J. Am. Chem. Soc.*, 2013, **135**, 1864–1871.

78 S. G. Minasian, J. M. Keith, E. R. Batista, K. S. Boland, S. A. Kozimor, R. L. Martin, D. K. Shuh, T. Tyliszczak and L. J. Vernon, *J. Am. Chem. Soc.*, 2013, **135**, 14731–14740.

79 S. G. Minasian, J. M. Keith, E. R. Batista, K. S. Boland, D. L. Clark, S. A. Kozimor, R. L. Martin, D. K. Shuh and T. Tyliszczak, *Chem. Sci.*, 2014, **5**, 351–359.

80 X.-D. Wen, M. W. Loeble, E. R. Batista, E. Bauer, K. S. Boland, A. K. Burrell, S. D. Conradson, S. R. Daly, S. A. Kozimor, S. G. Minasian, R. L. Martin, T. M. McCleskey, B. L. Scott, D. K. Shuh and T. Tyliszczak, *J. Electron Spectrosc. Relat. Phenom.*, 2014, **194**, 81–87.

81 S. E. Shadle, B. Hedman, K. O. Hodgson and E. I. Solomon, *Inorg. Chem.*, 1994, **33**, 4235–4244.

82 S. E. Shadle, B. Hedman, K. O. Hodgson and E. I. Solomon, *J. Am. Chem. Soc.*, 1995, **117**, 2259–2272.

83 T. Glaser, B. Hedman, K. O. Hodgson and E. I. Solomon, *Acc. Chem. Res.*, 2000, **33**, 859–868.

84 E. I. Solomon, B. Hedman, K. O. Hodgson, A. Dey and R. K. Szilagyi, *Coord. Chem. Rev.*, 2005, **249**, 97–129.

85 M. V. Ryzhkov, V. A. Gubanov, Y. A. Teterin and A. S. Baev, *Z. Phys. B: Condens. Matter*, 1985, **59**, 1–6.

86 M. V. Ryzhkov, V. A. Gubanov, Y. A. Teterin and A. S. Baev, *Z. Phys. B: Condens. Matter*, 1985, **59**, 7–14.

87 Y. N. Xu, Z. Q. Gu and W. Y. Ching, *Phys. Rev. B: Condens. Matter*, 1997, **56**, 14993–15000.

88 P. W. Peacock and J. Robertson, *J. Appl. Phys.*, 2002, **92**, 4712–4721.

89 H. B. Lal and K. Gaur, *J. Mater. Sci.*, 1988, **23**, 919–923.

90 A. V. Prokofiev, A. I. Shelykh and B. T. Melekh, *J. Alloys Compd.*, 1996, **242**, 41–44.

91 M. Humphries, Rare Earth Elements: The Global Supply Chain CRS Report R41347, Congressional Research Service, Washington DC, 2013.

92 A. Trovarelli, *Comments Inorg. Chem.*, 1999, **20**, 263–284.

93 A. Trovarelli, *Catal. Rev.*, 1996, **38**, 439–520.

94 G. Adachi and N. Imanaka, *Chem. Rev.*, 1998, **98**, 1479–1514.

95 V. V. Afanas'ev, M. Badylevich, A. Stesmans, A. Laha, H. J. Osten, A. Fissel, W. Tian, L. F. Edge and D. G. Schlom, *Appl. Phys. Lett.*, 2008, **93**, 192105.

96 V. Mikhelashvili, G. Eisenstein and F. Edelmann, *Appl. Phys. Lett.*, 2002, **80**, 2156–2158.

97 G. Seguini, E. Bonera, S. Spiga, G. Scarel and M. Fanciulli, *Appl. Phys. Lett.*, 2004, **85**, 5316–5318.

98 N. Singh, S. M. Saini, T. Nautiyal and S. Auluck, *J. Appl. Phys.*, 2006, **100**, 083525.

99 J.-L. Bridot, A.-C. Faure, S. Laurent, C. Riviere, C. Billotey, B. Hiba, M. Janier, V. Josserand, J.-L. Coll, L. Vander Elst, R. Muller, S. Roux, P. Perriat and O. Tillement, *J. Am. Chem. Soc.*, 2007, **129**, 5076–5084.

100 H. M. Crosswhite, H. Crosswhite, W. T. Carnall and A. P. Paszek, *J. Chem. Phys.*, 1980, **72**, 5103–5117.

101 T. R. Cundari and W. J. Stevens, *J. Chem. Phys.*, 1993, **98**, 5555–5565.

102 V. Vetere, P. Maldivi and C. Adamo, *J. Comput. Chem.*, 2003, **24**, 850–858.

103 L. Petit, A. Svane, Z. Szotek and W. M. Temmerman, *Phys. Rev. B: Condens. Matter*, 2005, **72**, 205118.

104 J. Y. Chan, S. M. Kauzlarich, P. Klavins, R. N. Shelton and D. J. Webb, *Chem. Mater.*, 1997, **9**, 3132–3135.

105 V. Fritsch, J. D. Thompson, J. L. Sarrao, H. A. K. von Nidda, R. M. Eremina and A. Loidl, *Phys. Rev. B: Condens. Matter*, 2006, **73**, 094413.

106 H. X. Mai, Y. W. Zhang, R. Si, Z. G. Yan, L. D. Sun, L. P. You and C. H. Yan, *J. Am. Chem. Soc.*, 2006, **128**, 6426–6436.

107 X. H. Chen, T. Wu, G. Wu, R. H. Liu, H. Chen and D. F. Fang, *Nature*, 2008, **453**, 761–762.

108 J. M. Veauthier, E. J. Schelter, C. N. Carlson, B. L. Scott, R. E. Da Re, J. D. Thompson, J. L. Kiplinger, D. E. Morris and K. D. John, *Inorg. Chem.*, 2008, **47**, 5841–5849.

109 B. L. Drake, F. Grandjean, M. J. Kangas, E. K. Okudzeto, A. B. Karki, M. T. Sougrati, D. P. Young, G. J. Long and J. Y. Chan, *Inorg. Chem.*, 2010, **49**, 445–456.

110 F. Wang, Y. Han, C. S. Lim, Y. Lu, J. Wang, J. Xu, H. Chen, C. Zhang, M. Hong and X. Liu, *Nature*, 2010, **463**, 1061–1065.

111 G. Wang, Q. Peng and Y. Li, *Acc. Chem. Res.*, 2011, **44**, 322–332.

112 K. V. Kaznatcheev, C. Karunakaran, U. D. Lanke, S. G. Urquhart, M. Obst and A. P. Hitchcock, *Nucl. Instrum. Methods Phys. Res., Sect. A*, 2007, **582**, 96–99.

113 A. L. D. Kilcoyne, T. Tyliszczak, W. F. Steele, S. Fakra, P. Hitchcock, K. Franck, E. Anderson, B. Harteneck, E. G. Rightor, G. E. Mitchell, A. P. Hitchcock, L. Yang, T. Warwick and H. Ade, *J. Synchrotron Radiat.*, 2003, **10**, 125–136.

114 V. M. Goldschmidt, F. Ulrich and T. Barth, *Skr. Nor. Vidensk.-Akad., [Kl.] 1: Mat.-Naturvidensk. Kl.*, 1925, **5**, 5–14.

115 I. Warshaw and R. Roy, *J. Phys. Chem.*, 1961, **65**, 2048–2051.

116 R. G. Haire and L. Eyring, in *Handbook on the Physics and Chemistry of Rare Earths*, ed. K. A. Gschneider, L. Eyring, G. R. Choppin and G. H. Lander, Elsevier Science, Amsterdam, 1994, vol. 18, pp. 413–505.

117 N. Hirosaki, S. Ogata and C. Kocer, *J. Alloys Compd.*, 2003, **351**, 31–34.

118 B. Wu, M. Zinkevich, F. Aldinger, D. Wen and L. Chen, *J. Solid State Chem.*, 2007, **180**, 3280–3287.

119 P. Aldebert and J. P. Traverse, *Mater. Res. Bull.*, 1979, **14**, 303–323.

120 B. Antic, M. Mitric and D. Rodic, *J. Magn. Magn. Mater.*, 1995, **145**, 349–356.

121 H. Barnighausen and G. Schiller, *J. Less-Common Met.*, 1985, **110**, 385–390.

122 A. M. Pires, M. R. Davolos, C. O. Paiva-Santos, E. B. Stucchi and J. Flor, *J. Solid State Chem.*, 2003, **171**, 420–423.

123 O. Greis, R. Ziel, B. Breidenstein, A. Haase and T. Petzel, *J. Alloys Compd.*, 1995, **216**, 255–258.

124 Z. Heiba, H. Okuyucu and Y. S. Hascicek, *J. Appl. Crystallogr.*, 2002, **35**, 577–580.

125 J. Blanusa, M. Mitric, D. Rodic, A. Szytula and M. Slaski, *J. Magn. Magn. Mater.*, 2000, **213**, 75–81.

126 V. Katari, S. N. Achary, S. K. Deshpande, P. D. Babu, A. K. Sinha, H. G. Salunke, N. Gupta and A. K. Tyagi, *J. Phys. Chem. C*, 2014, **118**, 17900–17913.

127 M. Mitric, J. Blanusa, T. Barudzija, Z. Jaglicic, V. Kusigerski and V. Spasojevic, *J. Alloys Compd.*, 2009, **485**, 473–477.

128 A. Saiki, N. Ishizawa, N. Mizutani and M. Kato, *J. Ceram. Soc. Jpn.*, 1985, **93**, 649–654.

129 E. N. Maslen, V. A. Streltsov and N. Ishizawa, *Acta Crystallogr., Sect. B: Struct. Sci.*, 1996, **52**, 414–422.

130 M. Guzik, J. Pejchal, A. Yoshikawa, A. Ito, T. Goto, M. Siczek, T. Lis and G. Boulon, *Cryst. Growth Des.*, 2014, **14**, 3327–3334.

131 M. Magnuson, S. M. Butorin, L. Werme, J. Nordgren, K. E. Ivanov, J. H. Guo and D. K. Shuh, *Appl. Surf. Sci.*, 2006, **252**, 5615–5618.

132 C. Fillaux, D. Guillaumont, J.-C. Berthet, R. Copping, D. K. Shuh, T. Tyliszczak and C. Den Auwer, *Phys. Chem. Chem. Phys.*, 2010, **12**, 14253–14262.

133 S. M. Butorin, D. K. Shuh, K. O. Kvashnina, J. Guo, L. Werme and J. Nordgren, *Anal. Chem.*, 2013, **85**, 11196–11200.

134 D. R. Mullins, S. H. Overbury and D. R. Huntley, *Surf. Sci.*, 1998, **409**, 307–319.

135 L. A. J. Garvie and P. R. Buseck, *J. Phys. Chem. Solids*, 1999, **60**, 1943–1947.

136 A. Harvey, B. Gu, I. Kennedy, S. Risbud and V. Leppert, *J. Phys.: Condens. Matter*, 2006, **18**, 2181–2189.

137 G. A. Botton, J. A. Gupta, D. Landheer, J. P. McCaffrey, G. I. Sproule and M. J. Graham, *J. Appl. Phys.*, 2002, **91**, 2921–2928.

138 M. Ou, V. Mauchamp, B. Mutelet, T. Epicier, J. C. Le Bosse, S. Roux, O. Tillement and P. Perriat, *J. Phys. Chem. C*, 2009, **113**, 4038–4041.

139 T. Epicier, J. C. Le Bosse, P. Perriat, S. Roux and O. Tillement, *Eur. Phys. J.: Appl. Phys.*, 2011, 54.

140 S. A. Kozimor, P. Yang, E. R. Batista, K. S. Boland, C. J. Burns, D. L. Clark, S. D. Conradson, R. L. Martin, M. P. Wilkerson and L. E. Wolfsberg, *J. Am. Chem. Soc.*, 2009, **131**, 12125–12136.

141 S. G. Minasian, J. M. Kieth, E. R. Batista, K. S. Boland, C. N. Christensen, D. L. Clark, S. D. Conradson, S. A. Kozimor, R. L. Martin, D. E. Schwarz, D. K. Shuh, G. L. Wagner, M. P. Wilkerson, L. E. Wolfsberg and P. Yang, *J. Am. Chem. Soc.*, 2012, **134**, 5586–5597.

142 I. Nishida, K. Tatsumi and S. Muto, *Mater. Trans.*, 2009, **50**, 952–958.

143 Z. Y. Wu, F. Jollet, S. Gota, N. Thromat, M. Gautier-Soyer and T. Petit, *J. Phys.: Condens. Matter*, 1999, **11**, 7185–7194.

144 H. Ishibashi, K. Shimomoto and K. Nakahigashi, *J. Phys. Chem. Solids*, 1994, **55**, 809–814.

145 F. Jollet, C. Noguera, N. Thromat, M. Gautier and J. P. Duraud, *Phys. Rev. B: Condens. Matter*, 1990, **42**, 7587–7595.

146 L. Douillard, M. Gautier, N. Thromat, M. Henriot, M. J. Guittet, J. P. Duraud and G. Tourillon, *Phys. Rev. B: Condens. Matter*, 1994, **49**, 16171–16180.

147 J. W. Allen, *J. Magn. Magn. Mater.*, 1985, **47–8**, 168–174.

148 E. Wuilloud, B. Delley, W. D. Schneider and Y. Baer, *Phys. Rev. Lett.*, 1984, **53**, 2519–2519.

149 J. C. Slater, *Phys. Rev.*, 1930, **36**, 57–64.

150 L. Brewer, *J. Opt. Soc. Am.*, 1971, **61**, 1666–1682.

151 W. C. Martin, R. Zalubas and L. Hagan, *Atomic Energy Levels – The Rare Earth Elements NSRDS-NBS 60*, U.S. Department of Commerce, Washington, DC, 1978.

152 S. R. Daly, J. M. Keith, E. R. Batista, K. S. Boland, D. L. Clark, S. A. Kozimor and R. L. Martin, *J. Am. Chem. Soc.*, 2012, **134**, 14408–14422.

153 M. Gasgnier, G. Schiffmacher, P. Caro and L. Eyring, *J. Less-Common Met.*, 1986, **116**, 31–42.

154 A. T. Wen and A. P. Hitchcock, *Can. J. Chem.*, 1993, **71**, 1632–1644.

155 M. Casarin, P. Finetti, A. Vittadini, F. Wang and T. Ziegler, *J. Phys. Chem. A*, 2007, **111**, 5270–5279.

156 M. R. MacDonald, J. E. Bates, M. E. Fieser, J. W. Ziller, F. Furche and W. J. Evans, *J. Am. Chem. Soc.*, 2012, **134**, 8420–8423.

157 M. R. MacDonald, J. E. Bates, J. W. Ziller, F. Furche and W. J. Evans, *J. Am. Chem. Soc.*, 2013, **135**, 9857–9868.

158 C. M. Kotyk, M. R. MacDonald, J. W. Ziller and W. J. Evans, *Organometallics*, 2015, **34**, 2287–2295.

159 M. R. MacDonald, M. E. Fieser, J. E. Bates, J. W. Ziller, F. Furche and W. J. Evans, *J. Am. Chem. Soc.*, 2013, **135**, 13310–13313.

160 R. R. Langeslay, M. E. Fieser, J. W. Ziller, F. Furche and W. J. Evans, *Chem. Sci.*, 2015, **6**, 517–521.

161 H. S. La Pierre, A. Scheurer, F. W. Heinemann, W. Hieringer and K. Meyer, *Angew. Chem., Int. Ed.*, 2014, **53**, 7158–7162.

162 N. Kaltsoyannis, *Inorg. Chem.*, 2013, **52**, 3407–3413.

163 M. L. Neidig, D. L. Clark and R. L. Martin, *Coord. Chem. Rev.*, 2013, **257**, 394.

164 G. Meyer, *Angew. Chem., Int. Ed.*, 2014, **53**, 3550–3551.

165 G. Brauer, *Handbook of Preparative Inorganic Chemistry*, Academic Press, New York, 2nd edn, 1963.

166 M. Gasgnier, G. Schiffmacher, L. Albert, P. E. Caro, H. Dexpert, J. M. Esteva, C. Blancard and R. C. Karnatak, *J. Less-Common Met.*, 1989, **156**, 59–73.

167 N. Baenziger, H. S. Schuldt, L. Eyring and H. A. Eick, *J. Am. Chem. Soc.*, 1961, **83**, 2219–2223.

168 K. R. Meihaus, S. G. Minasian, W. W. Lukens Jr., S. A. Kozimor, D. K. Shuh, T. Tyliszczak and J. R. Long, *J. Am. Chem. Soc.*, 2014, **136**, 6056–6068.

169 A. B. Altman, C. D. Pemmaraju, C. Camp, J. Arnold, S. G. Minasian, D. Prendergast, D. K. Shuh and T. Tyliszczak, *J. Am. Chem. Soc.*, 2015, **137**, 10304–10316.

170 T. C. Weng, G. S. Waldo and J. E. Penner-Hahn, *J. Synchrotron Radiat.*, 2005, **12**, 506–510.

171 S. D. George, P. Brant and E. I. Solomon, *J. Am. Chem. Soc.*, 2005, **127**, 667–674.

172 L. R. Morss, in *Handbook on the Physics and Chemistry of Rare Earths*, ed. K. A. Gschneider, L. Eyring, G. R. Choppin and G. H. Lander, Elsevier Science, Amsterdam, 1994, vol. 18, pp. 239–291.

173 L. J. Nugent, J. L. Burnett and L. R. Morss, *J. Chem. Thermodyn.*, 1973, **5**, 665–678.

174 E. H. P. Cordfunke and R. J. M. Konings, *Thermochim. Acta*, 2001, **375**, 65–79.